NJC

ROYAL SOCIETY OF CHEMISTRY

PAPER

View Article Online
View Journal

Cite this: DOI: 10.1039/d5nj03536h

Enhanced photocatalytic activity of g-C_3N_4 modified BiOBr for the degradation of reactive blue 19 under visible light

Kamya Jasuja[a] and Raj Kumar Das *[ab]

Nowadays, the concentration of dyes in water is elevated as a consequence of unregulated disposal, which leads to water contamination. To mitigate their detrimental effects, effective elimination is crucial. In this regard, g-C_3N_4/BiOBr was synthesised *via* a hydrothermal technique to examine the visible light-driven photocatalytic decomposition of reactive blue 19 (RB19). The synthesised catalyst was characterised using multiple techniques, such as diffuse reflectance spectroscopy (DRS), high-resolution transmission electron microscopy (HRTEM), field emission scanning electron microscopy (FESEM), X-ray diffraction (XRD), X-ray photoelectron spectroscopy (XPS), electrochemical impedance spectroscopy (EIS), and photoluminescence (PL) spectroscopy. The degradation efficiency of 10 wt% g-C_3N_4-loaded BiOBr towards RB19 in the presence of visible light was observed to be 89% within 240 min under visible light. Moreover, control experiments validate the involvement of superoxide anions ($O_2^{\bullet-}$), hydroxyl radicals ($^{\bullet}OH$), and holes (h^+) in the photocatalytic degradation pathway. The calculated band positions support the formation of Z-scheme-type heterojunctions. In addition, the high-resolution mass spectrometry (HR-MS) analysis confirms the existence of small fragments (*m*/*z* = 184, 202, *etc.*), hence validating the photodegradation process. Moreover, the synthesised catalyst demonstrates remarkable stability and reusability. Moreover, the photocatalytic degradation efficiency in different water samples, including deionised water, RO water, and tap water, was found to be practically similar. Consequently, the photocatalyst can effectively eliminate the harmful pollutants present in wastewater.

Received 3rd September 2025,
Accepted 25th November 2025

DOI: 10.1039/d5nj03536h

rsc.li/njc

Introduction

The textile sector is well known for its substantial usage of hazardous and non-biodegradable pigments in its manufacturing processes.[1] These chemical species are highly mutagenic, teratogenic, and carcinogenic.[2] Annually, on a global scale, around 50 000 tonnes of dyes are discharged into the environment, causing serious health problems like nausea, skin infections, vomiting, and liver and kidney-related problems and having a harmful influence on aquatic life.[3–5] Furthermore, synthetic dyes, which are found in many industrial wastewater streams, are highly stable molecules that are difficult to disintegrate using conventional physicochemical techniques. Due to their harmful effects, these toxic pollutants must be removed before discharge.[6] Reactive blue 19 is a reactive dye that is based on anthraquinone vinyl sulphone and is widely used in the textile industry to dye cellulose fibres, such as cotton.[7,8] It forms a strong covalent bond with fibers due to its moisture fastness. Unfortunately, effluents include large concentrations of unstitched dye, which is stable and non-biodegradable, inhibiting microbial growth and increasing environmental consequences.[9,10] Therefore, it is essential to eliminate these contaminants from effluents. Various methods were investigated for the eradication of pollutants, such as coagulation, microfiltration, adsorption, ion-exchange, and photocatalysis. One of the highly potential technologies is photocatalytic degradation, which completely decomposes the pollutant rather than converting it to a different form. The photocatalytic degradation driven by visible light using several types of semiconductors has seen an extensive rise in recent years as a result of its affordability, ecological sustainability, and efficacy.[11,12] Bismuth oxyhalide-based materials, BiOX (X = Cl, Br, I, and F), exhibit exceptional degradation efficacy under visible light. BiOBr is the most effective among numerous bismuth oxyhalides due to a smaller band gap, distinctive structure and significant capacity to adsorb visible light.[13,14] However, the high recombination rate of photo-excited charge carriers renders BiOBr insufficient for the optimum extent of pollutant degradation. Several methods, such as semiconductor modification and elemental doping, may be

[a] *Department of Chemistry and Biochemistry, Thapar Institute of Engineering & Technology, Patiala-147004, Punjab, India. E-mail: rkdas@thapar.edu*
[b] *TIET-Virginia Tech Center of Excellence in Emerging Materials, Thapar Institute of Engineering and Technology, Patiala, 147004, India*

implemented to reduce the recombination rate.[15,16] One of the efficient methods is the modification of semiconductors by incorporating g-C_3N_4 with BiOBr. Polymeric semiconductor graphitic carbon nitride is composed of a 2D layered structure. g-C_3N_4 is an excellent material among other semiconductors owing to its greater surface area, substantial thermal stability, reduced cost, lower toxicity, and narrower band gap.[17–19] The degradation efficiency is improved by suppressing the recombination rate through the combination of two semiconductors with appropriate band gaps, thereby increasing the overall degradation efficiency. For instance, Fahad and coworkers synthesized g-C_3N_4/$GdVO_4$ for the degradation of amaranth and reactive red 2.[20] TiO_2/g-C_3N_4 was synthesized by Abdul and his coworkers for the degradation of congo red.[21] Hassanzadeh *et al.* synthesised g-C_3N_4/$CoFe_2O_4$ by using the hydrothermal method and investigated its performance towards the visible light-driven elimination of methylene blue, rhodamine B, and methyl orange.[22]

The hydrothermal approach was used by Li and coworkers to synthesise BiOBr/ZnO, which was then modified by H_2/Ar low-temperature plasma. Using a 250 W xenon lamp, 76% of methyl orange was photocatalytically degraded in 120 minutes.[23] A 300 W xenon lamp was used to test the photocatalytic degradation of RhB in 70 minutes after Guo *et al.* synthesised BiOBr using a one-pot solvothermal method.[24] Wu and coworkers synthesised BiOCl@WS_2 using a precipitation method; they examined the photocatalytic degradation of MO, RhB, and CV. Using a 500-W xenon lamp, they were able to achieve 81%, 100%, and 95% degradation, respectively, in 120 minutes.[25] By synthesizing Ag-BiOBr, the photocatalytic degradation of RhB was investigated; the degradation efficiency was found to reach 97.5% in 40 minutes.[26] The BiOCl/Ag/WO_3 nanocomposite was prepared *via* a laser ablation method. The ternary composite's ability to degrade MB photocatalytically was investigated. It was discovered that, with 200 mW of light intensity, the degradation efficiency was 74% in 120 minutes.[27] Due to the structural complexity and high stability of RB19, the photocatalytic elimination is a highly complicated procedure. Most of the reported catalysts are effective only at low pollutant concentrations and high light intensities.[28–31] The principal goal of the current work was to explore the removal of reactive blue 19 using a non-toxic, low-cost, and highly efficient photocatalyst through the utilisation of the hydrothermal manufacturing process. Using the hydrothermal approach, this work involves the synthesis of g-C_3N_4/BiOBr with varying weight percentages, as well as the evaluation of the degradation efficiency towards reactive blue 19. This prepared catalyst (g-C_3N_4/BiOBr) degrades high concentration (60 ppm) of pollutant with a lower intensity (50 Wm^{-2}) of light.

Materials and methods

Chemicals and reagents used

Cetyltrimethyl ammonium bromide (CTAB) [$C_{19}H_{42}BrN$] 99% AR, bismuth nitrate pentahydrate [Bi $(NO_3)_3{\cdot}5H_2O$], ethanediol, 99.5% AR, and melamine [$C_3H_6N_6$] extra pure were obtained from Loba Chemie Pvt. Ltd. Reactive blue 19 (RB19) was acquired from the Sisco Research Laboratory (SRL), India. Pure ethanol (99%) was purchased from Changshu Hongsheng Fine Chemicals Co., Ltd. A Milli-Q, Millipore ultrafiltration system was employed to produce deionised water (DI). Polyvinylidene fluoride (PVDF) and carbon black (CB) were obtained from Sigma Aldrich and Nanoshell, respectively. Fluorinated tin oxide (FTO) glasses (with a resistance of less than 10 Ω) were acquired from Vritra Technologies.

Preparation of g-C_3N_4

For synthesizing graphitic carbon nitride, in a vessel, melamine (5 g) was taken, which was heated at 550 °C for 4 hours, with a heating rate of 2 °C min^{-1}.[32] Upon completion of the reaction, it was cooled to room temperature. The final product was yellow in colour, designated as gCN.

Preparation of BiOBr and g-C_3N_4-loaded BiOBr

To synthesize g-C_3N_4/BiOBr, 1.5 mmol (0.727 g) of [Bi $(NO_3)_3{\cdot}5H_2O$] and a specified quantity of g-C_3N_4 were mixed in 40 mL of ethanediol and sonicated for 30 minutes to obtain solution A. Moreover, to prepare solution B, 1.5 mmol (0.546 g) of CTAB was incorporated into 40 mL of DI and stirred for 30 minutes. Subsequently, solution B was introduced into solution A. The final suspension was then stirred for an additional half an hour. The reaction mixture was then autoclaved for 12 hours at 160 °C.[33] Following the reaction, the solution was washed with ethanol and water, followed by drying at 60 °C to obtain the required products, designated as GB5, GB10, and GB15 (5, 10, and 15 represent the percentage of g-CN loading on BiOBr). The synthesis of pure BiOBr was performed under the same conditions without adding gCN.

Preparation of thin films

To conduct electrochemical impedance spectroscopy (EIS), working electrodes were prepared by utilizing a drop-casting technique. A homogeneous paste was made by combining PVDF (1 mg) with NMP (40–60 μL). Furthermore, CB (1 mg) was incorporated and subsequently mixed for 15–20 minutes. Afterwards, 8 mg of the produced sample (BiOBr and GB10) was included, affording a homogeneous suspension. Following that, the mixture was drop-cast onto FTO and later dried at 80 °C for 12 hours.

Characterization

To scrutinize the physicochemical properties, structure, shape, and internal composition of the prepared sample, a variety of characterization methods were carried out. A Shimadzu UV-1900 UV-visible spectrophotometer was utilized to ascertain the diffuse reflectance spectra (DRS). The diffraction patterns were verified utilizing X-ray diffraction (XRD) with an X'Pert Pro 24 Cu-Kα (1.54 Å) with an angle of 2θ of 5–90° and operating at 45 kV. To investigate the surface shape of the synthesized samples, field emission scanning electron microscopy (FESEM, Carl-Zeiss Sigma 500) and energy dispersive spectroscopy (EDS) were used. Additionally, to get a deeper understanding of the

morphology of the samples, high-resolution transmission electron microscopy (HRTEM) was performed by using a JEOL JEM 2100 plus. X-ray photoelectron spectroscopy (XPS) was used to determine the oxidation states of the material. Moreover, to detect the functional groups, Fourier transmission infrared (FTIR, IR Tracer-100, Shimadzu) spectroscopy was used. Furthermore, high-resolution mass spectrometry (HR-MS) was employed to analyse the fragments, using the Waters QTOF mass spectrometer, Xevo G2-XS, equipped with a UHPLC system and integrated ESI and APCI ionization sources. A Biologic VSP300 potentiostat was employed to conduct EIS experiments under dark at 0.80 V *vs.* RHE, with a frequency range of 1–10^5 Hz. The electrode system comprises three sets of electrodes: a standard calomel electrode, a platinum (Pt) electrode, and a sample mounted on FTO glass. These electrodes serve as the reference, counter, and working electrodes, and 0.1 M sodium sulphate as the electrolyte.

Photocatalytic degradation studies

The prepared samples were examined for their ability to eliminate RB19 under the irradiation of visible light. Firstly, 10 mL of pollutant containing 10 mg of the prepared photocatalyst was placed under dark conditions for 0.5 hours to ascertain the adsorption–desorption equilibrium. Afterwards, the test tubes were exposed to light using a B22-50W LED Wipro Garnet LED (light intensity = 5000 lumens and wavelength $>$ 360 nm) for 240 minutes. Subsequently, the reaction mixture was subjected to centrifugation for the separation of the catalyst. The dye concentration was subsequently determined by recording the absorbance at 590 nm.

The degradation efficacy was determined by using the following equation (eqn (1)):

$$\text{Photocatalytic degradation efficiency}\,(\%) = \frac{A_0 - A}{A_0} \times 100\% \quad (1)$$

where A_0 and A represent the initial and final absorbances of the solution.

Results and discussion

DRS studies

To analyze the optical characteristics of pure BiOBr, gCN, and their hybrid composites, DRS was utilized. The absorption edge values of gCN and BiOBr were observed to be 450 nm and 476 nm, respectively,[34,35] as depicted in Fig. 1(a). Additionally, from Tauc's plot, the band gap values for gCN and BiOBr were determined as 2.60 eV and 2.51 eV, respectively. The minimum band gap values decrease from 2.51 eV to 2.41 eV as the loading of gCN increases, as in Fig. 1(b). This clearly indicates the significant light absorption by gCN, which subsequently increases the overall efficiency. Additionally, the band gap at absorption

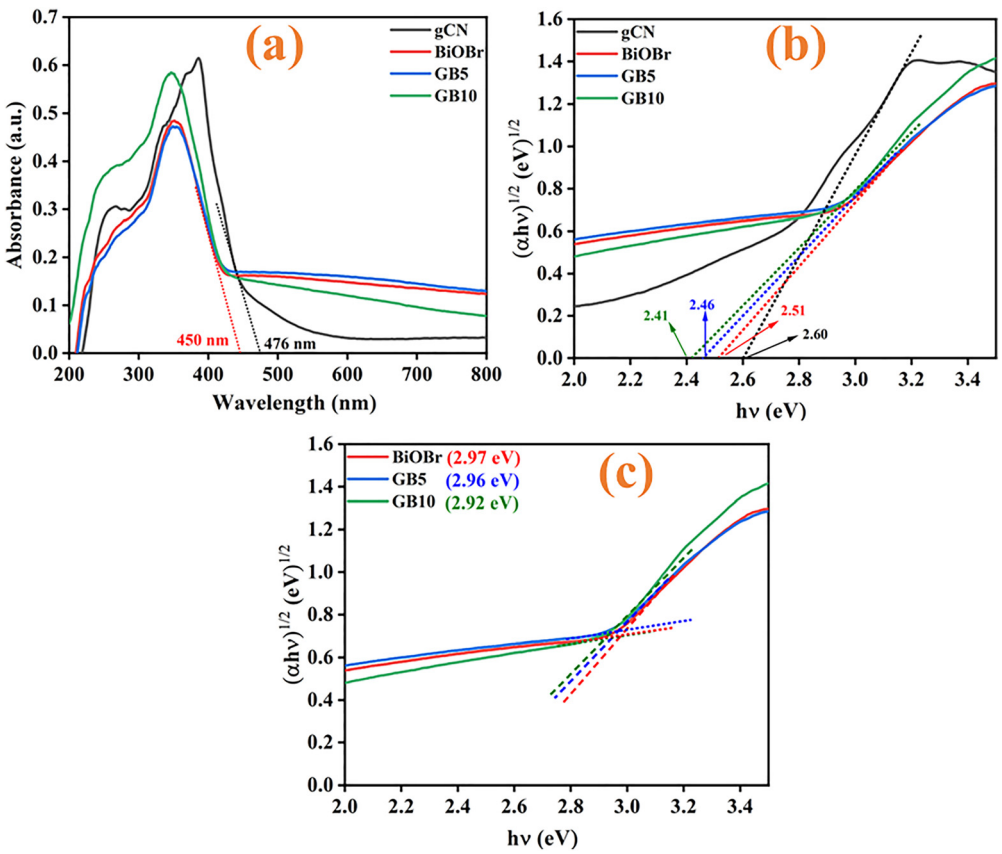

Fig. 1 (a) DRS of gCN, BiOBr, and their nanocomposites, (b) the minimum band gap, and (c) the band gap at the absorption edge band.

edge values was determined to be practically constant (2.92 eV to 2.97 eV), suggesting the structural stability upon adding gCN to BiOBr as presented in Fig. 1(c).

XRD analysis

This technique was employed to affirm the structural integrity of the prepared materials. The peaks observed at 10.86°, 21.80°, 25.19°, 31.72°, 32.22°, 39.38°, 46.29°, 57.22°, 67.52°, and 76.82° correspond to the (001), (002), (101), (102), (110), (112), (200), (212), (220), and (310) planes, respectively. This indicates tetragonal symmetry, which is supported by ICDD no. 09-0393.[36,37]

Moreover, the in-plane structure and two-dimensional packaging are responsible for the peaks observed at 13.1°, which correspond to the (100) plane. Furthermore, the peak at 27.5° is a result of the π stacking system for the interlayer face-to-face interactions and corresponds to the (002) plane. This corresponds precisely to ICDD no. 87-1526. Additionally, there is a minor displacement in the (002) peak in accordance with the alteration in the interplanar distance between the graphitic nitride sheets.[38] Furthermore, the diffraction pattern of the composites (GB5 and GB10) was identical to that of BiOBr, as illustrated in Fig. 2. This observation plainly indicates the structural integrity and stability of the composites.

The diffraction pattern of composites (GB5 and GB10) did not exhibit the characteristic peak of g-CN, which is due to lower loading and smaller X-ray coefficient.[39] Additionally, the crystallite size was calculated by using the Debye–Scherrer equation.[40] Moreover, the percentage (%) of crystallinity was also calculated for gCN, BiOBr, GB5, and GB10

$$D = \frac{K\lambda}{\beta \cos\theta} \quad (2)$$

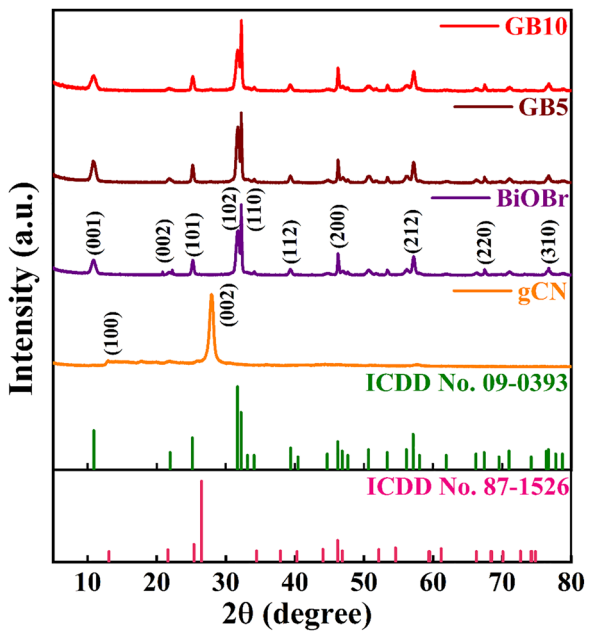

Fig. 2 XRD analysis of gCN, BiOBr, GB5, and GB10.

Table 1 Different crystallographic parameters of the synthesized samples

S. no.	Samples	Crystallite size (nm)	% Crystallinity
1.	gCN	10.5	32.4
2.	BiOBr	19.3	63.3
3.	GB5	22	61.9
4.	GB10	17.3	61.4

where K denotes the Scherrer constant and has a value of 0.9. The full width at half maxima at Bragg's diffraction angle θ is denoted by β.

$$\text{Crystallinity}\,(\%) = \frac{\text{crystalline spikes area}}{\text{overall area}} \times 100 \quad (3)$$

It was found that gCN has a smaller crystallite size, *i.e.*, 10.5 nm, whereas the crystallite sizes of BiOBr, GB5, and GB10 range from 17 to 20 nm. Furthermore, the percentages of crystallinity for gCN, BiOBr, GB5, and GB10 are 32.4%, 63.3%, 61.9%, and 61.4%, respectively (Table 1).

Importantly, the crystallinity and crystallite size of g-CN are smaller compared to the others, and the composites have a similar degree of crystallinity to the bare BiOBr. Such observation is consistent with the low X-ray scattering coefficient of g-CN compared to that of BiOBr.

FTIR studies

The formation of the hybrid composites was verified utilizing FTIR analysis. The signals detected at 513 cm^{-1} and 701 cm^{-1} correlate to the Bi–O symmetric stretching mode.[41] Additionally, the peaks within the range of 1000–1800 cm^{-1} were ascribed to heterocyclic C–N linkages and the Bi–Br band of BiOBr.[42] The extensive peak detected in the range of 3000–3500 cm^{-1} (Fig. 3) resulted from the O–H and N–H groups of gCN. The peak at 806 cm^{-1} correlates to the out-of-plane bending mode vibrations of heptazine units.[43] Following the coupling of gCN and BiOBr, the peaks retain similarities to the distinctive peaks of the

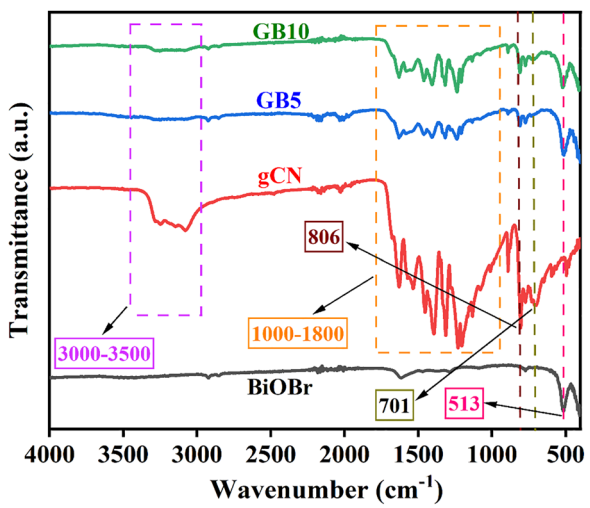

Fig. 3 FTIR spectra of gCN, BiOBr, GB5, and GB10.

bare materials, indicating an adequate integration inside the nanocomposite.

XPS analysis

The chemical state and atomic composition of BiOBr, gCN, and GB10 were evaluated using the XPS technique. The survey analysis, Fig. S1a, reveals the presence of Bi, O, and Br. The signals observed at 156.3 eV, 158.4 eV, 161.7 eV, and 163.4 eV in Fig. S1b depict the existence of Bi^0 and Bi^{3+}. This is because during preparation, the bromide interacts with the BiOBr surface, causing the reduction of Bi^{3+} to afford Bi^0. Furthermore, in the O 1s spectrum in Fig. S1c, the signals observed at 529.3 eV and 531.2 eV correspond to hydroxyl oxygen and lattice oxygen, respectively. Moreover, in Br 3d spectra in Fig. S1d, the signals observed at 67.4 eV and 68.4 eV may be due to Br^- ions.[44] Additionally, the XPS analysis of gCN confirms the successful synthesis of the material. In Fig. S2b, the peaks observed at 283.9 eV, 287.3 eV and 292.6 eV were due to graphitic carbon

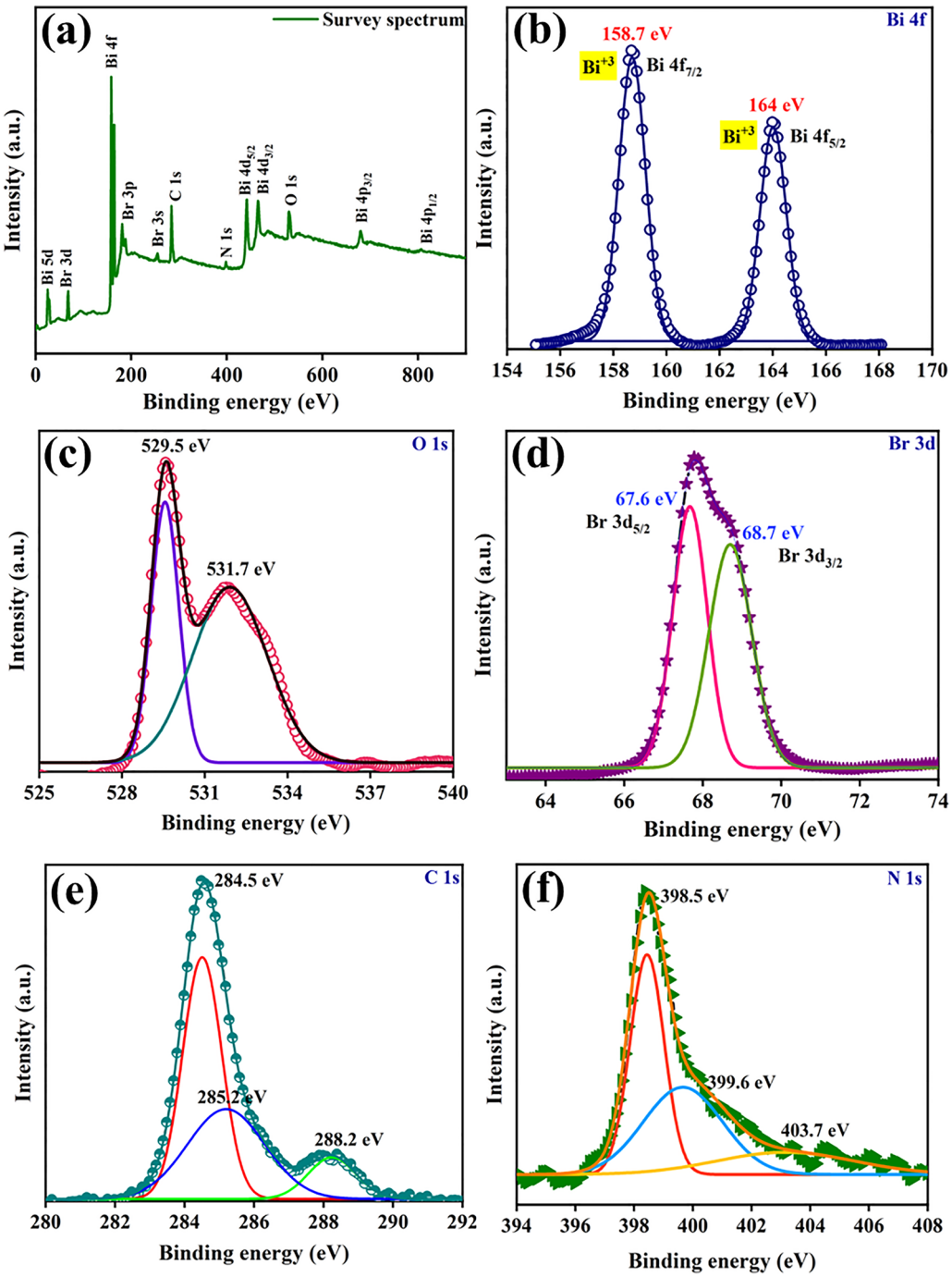

Fig. 4 XPS spectrum of GB10: (a) survey spectrum, (b) Bi [4f], (c) O [1s], (d) Br [3d], (e) C [1s], and (f) N [1s].

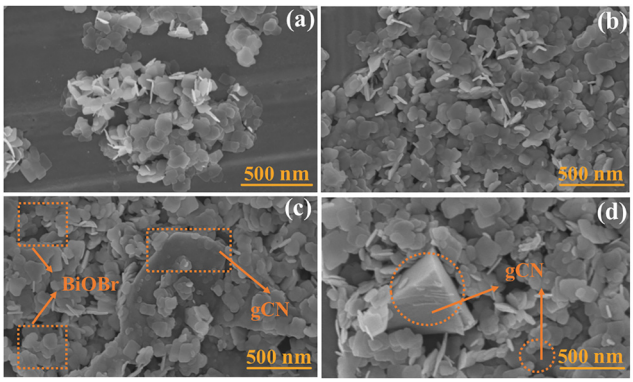

Fig. 5 (a) and (b) FESEM micrographs of BiOBr and (c) and (d) GB10.

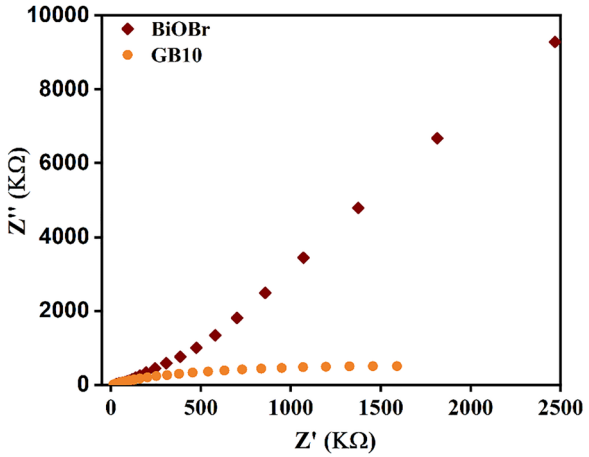

Fig. 7 Nyquist plots of BiOBr and GB10.

adsorbed on the surface, N=C–N groups of triazine rings and the $(N)_2$–C=N heterocyclic ring. Additionally, in the N 1s scan (Fig. S2) three peaks observed at 397.7 eV, 399.8 eV, and 403.7 eV were due to sp^2-bonded carbon and C–N–H and C≡N bonds respectively.[45]

The survey analysis, Fig. 4(a), showed that GB10 comprised all of the constituent elements, including Bi, O, Br, C, and N. The two signals detected at 158.7 eV and 164 eV confirm the existence of Bi^{3+} in the composite and the Bi^0 peak disappeared. Such observation can be attributed to the fact that the loading of g-CN on the BiOBr surface protects it from bromide, thereby inhibiting the reduction of Bi^{3+} [46] (Fig. 4b).

Furthermore, the signals at 529.5 eV and 531.7 eV were identified as due to the Bi–O linkage and surface O–H interactions, respectively.[47] Furthermore, in the Br spectra, the peaks observed at 68.7 eV and 67.6 eV, as seen in Fig. 4(c), are induced by Br $3d_{3/2}$ and Br $3d_{5/2}$, respectively (Fig. 4d).[48] In addition, the spectra of N 1s reveal three peaks centred at 398.5 eV, 399.6, and 403.7 eV, which were ascribed to bridged nitrogen atoms N–$(C)_3$, C–N=C bonds, and π excitations, respectively,[49] as shown in Fig. 4(f). Furthermore, in the C 1s spectrum, the signal at 284.5 eV is owing to extraneous carbon, while the peak observed at 285.2 eV is due to N–C=N linkages, and the peak at 288.2 eV is due to the $(N)_2$–C=N heterocyclic ring,[50] as depicted in Fig. 4e. The intensity of the peak centered at 284.5 eV increases as compared to the bare g-CN. Such observations support the successful synthesis of the composite.

Morphology

The morphology of the synthesised photocatalyst was analyzed using FESEM. The results indicate that BiOBr demonstrates sheet-like morphology (Fig. 5(a and b)).[51] Moreover, Fig. S3 clearly shows the layered structure of gCN. Additionally, as presented in Fig. 5(c and d), the co-existence of gCN and BiOBr clearly shows the successful fabrication of the nanocomposite. Furthermore, EDS mapping (Fig. S4) was employed to ascertain the elemental composition, revealing a uniform distribution of elements on the surface of the material and confirming the non-existence of any extra elements in the processed sample. HRTEM was utilized to provide a comprehensive understanding of the internal structure of the prepared photocatalyst. Fig. 6(a and d) depicts the effective integration of gCN and BiOBr,[52,53] signifying the presence of both bare materials. Furthermore, the fringe width measured 0.27 nm,[54]

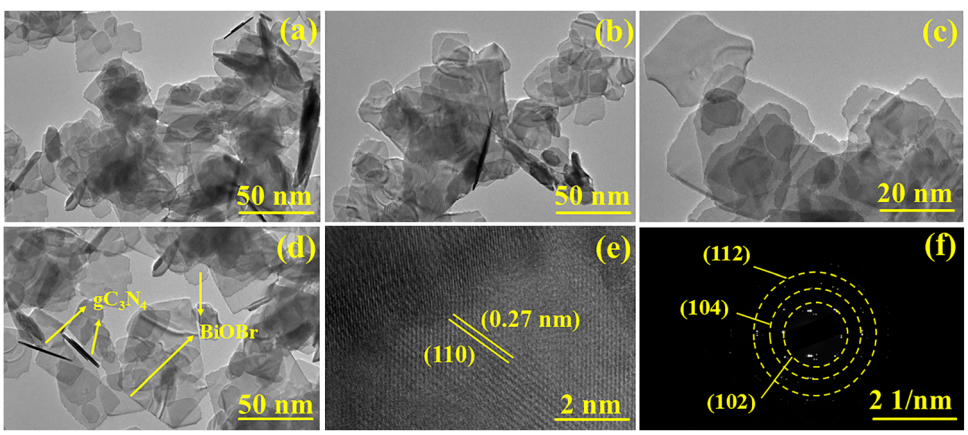

Fig. 6 HRTEM images of GB10 showing (a)–(d) the structural morphologies, (e) lattice fringes, and (f) selected area diffraction pattern of the synthesized catalyst.

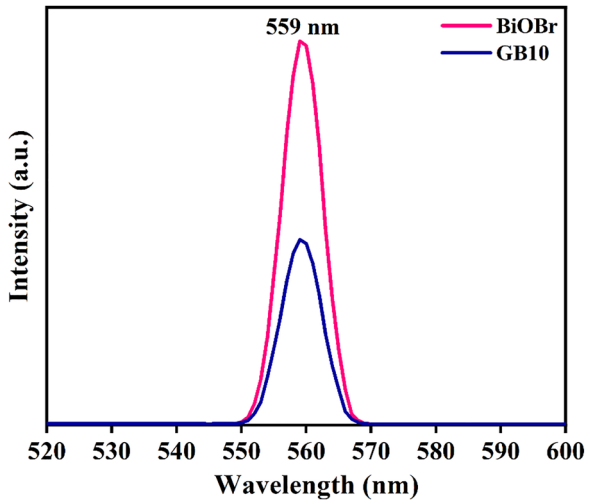

Fig. 8 PL spectra of BiOBr and GB10.

corresponding to the crystallographic (110) plane of BiOBr, indicating the persistence of structural stability inside the composite (Fig. 6e). Furthermore, to verify the crystallinity and stability, the SAED pattern was analysed, revealing concentric rings with light spots that match precisely crystallographic planes (102), (104), and (112), indicative of the tetragonal symmetry of BiOBr[55] (Fig. 6f).

EIS studies

The migration performance of photogenerated charge carriers was analyzed using electrochemical impedance spectroscopy. The BiOBr and GB10 studies were carried out in the absence of light. To understand the variation in the charge transfer properties upon gCN loading, the radius was calculated as seen in Fig. 7. In this case, more effective charge transfer and reduced impedance are reflected by smaller radii.[56] The results demonstrate that the EIS Nyquist plot of GB10 has a smaller radius than that of pure BiOBr, indicating that the loading of gCN facilitates the charge transport process. Consequently, GB10 can act as a more effective photocatalyst than pure BiOBr.

PL studies

The charge carrier recombination was scrutinized using photoluminescence spectra. Fig. 8 shows that GB10 has a lower intensity than BiOBr. Such observations suggest the successful loading of g-C_3N_4 on BiOBr, which reduces the recombination rate and hence boosts the degradation efficiency.[57] Consequently, GB10 heterostructures can be superior to bare materials in terms of their photocatalytic properties.

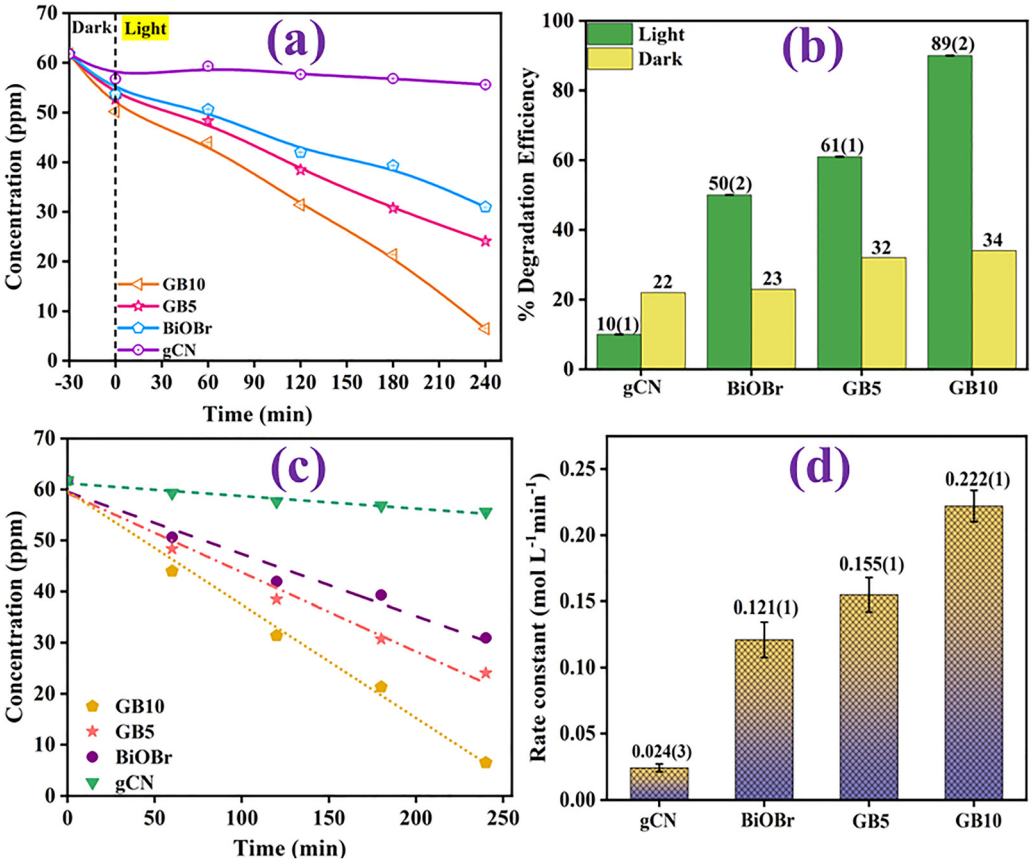

Fig. 9 (a) Degradation efficiency of RB19 with respect to time for all prepared samples, (b) comparative analysis of degradation efficacy under dark and light, (c) fitting of pseudo-zero order kinetic model, and (d) bar plot for rate constant values.

Photocatalytic degradation analysis

To evaluate the photocatalytic performance of gCN, BiOBr, and their composites in the presence of visible light irradiation towards RB19. To achieve an adsorption–desorption equilibrium, the mixture was initially placed in the dark for 30 minutes. Afterwards, the resultant suspension was irradiated with visible light for a period of 240 minutes. As evidenced by the results, it was observed that gCN and BiOBr exhibit a lower degradation efficiency as a result of reduced electron–hole pair recombination. This results in reduction in the maximum number of photogenerated charge carriers, which in turn limits the degradation efficiency to its optimal level. Moreover, the incorporation of gCN in GB5 resulted in a higher efficiency than BiOBr, as it facilitated the transfer of charge and generated photoexcited charge carriers, thereby increasing the degradation efficiency. Furthermore, GB10 exhibits the highest degradation efficiency (89%) as the concentration of gCN increases to 10% (Fig. 9(a–c), Fig. S5, and Table S1).

Additionally, the efficiency was evaluated in the dark for the optimal duration, and it was determined that the maximum efficiency for GB10 was 34%. Furthermore, the pseudo-zero-order model (eqn (4)) defines all photocatalytic degradation reactions.

$$C_t = C_0 - kt \quad (4)$$

where C_0 and C_t represent the initial and final concentrations and k represents the rate constant. In addition, the pseudo-zero-order kinetic model was additionally confirmed by half-life values (Fig. S6). The half-life values are found to be directly proportional to the initial concentration, which is consistent with the zero-order kinetic model. Also, it was noted that GB10 has the maximum rate constant of 0.222(1) mol L^{-1} min^{-1} (Fig. 9d).

The impact of time, quantity, and wt% loading was examined in order to optimise reaction conditions. The outcomes indicated that the degradation efficiency increases as the quantity of catalyst increases up to 10 mg. However, the efficiency decreased thereafter due to the blockage of the active sites, as presented in Fig. 10. Furthermore, no substantial increase was observed if the time was extended up to 5 hours (Fig. 10b). Additionally, the degradation efficiency decreased as the quantity of gCN loading on BiOBr exceeded 10% (Fig. 10c). In addition, to check the practical utility, RB19 solutions in RO water (Thapar University, Patiala, Punjab), tap water (bus stand area, Patiala, Punjab), and distilled water were tested and the photocatalytic efficiencies were examined under the analogous reaction conditions. It was observed that the degradation efficiency was practically similar in all different water samples, indicating that the catalyst is efficient for treating wastewater, as shown in Fig. 10d and Fig. S6.

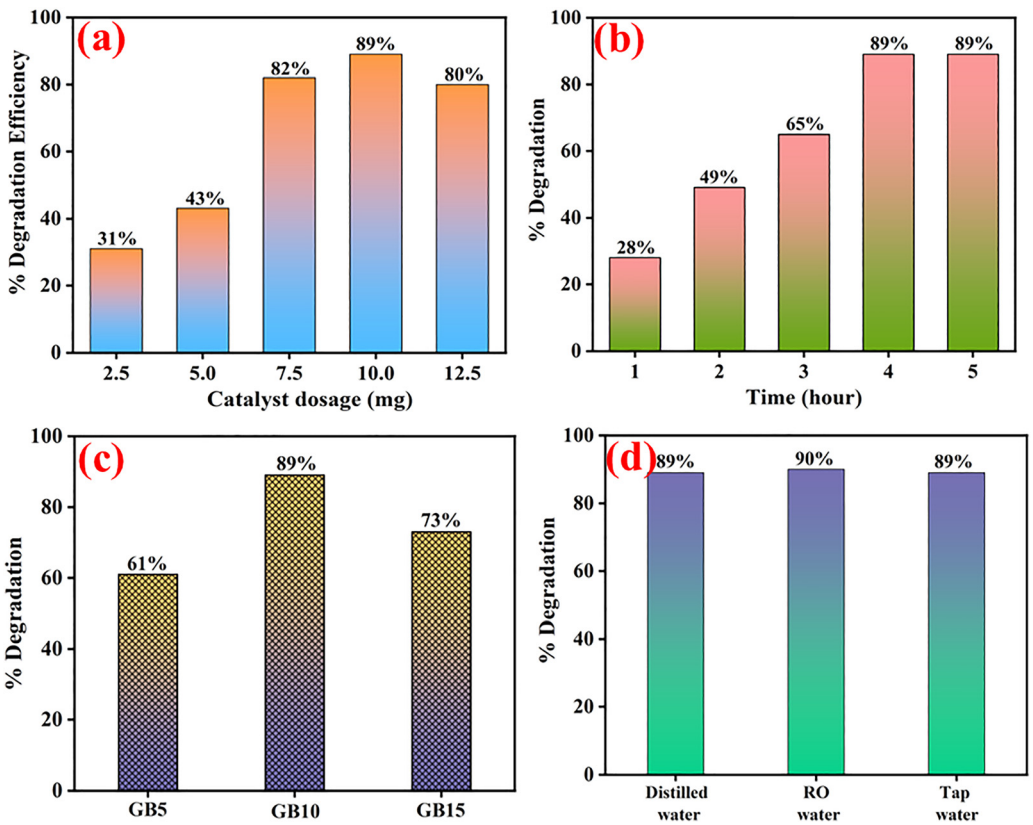

Fig. 10 Effect of reaction conditions: (a) amount of catalyst, (b) time of contact, (c) loading of gCN over BiOBr towards reactive blue 19, and (d) degradation efficiency in different water samples.

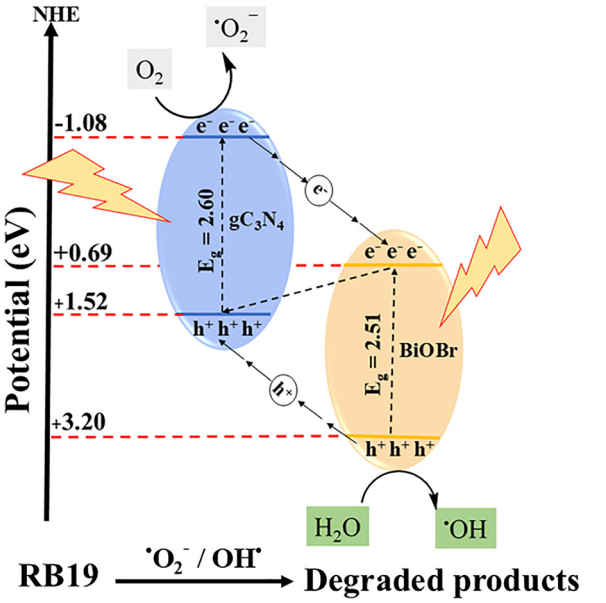

Fig. 11 Proposed mechanistic representation for the degradation of RB19.

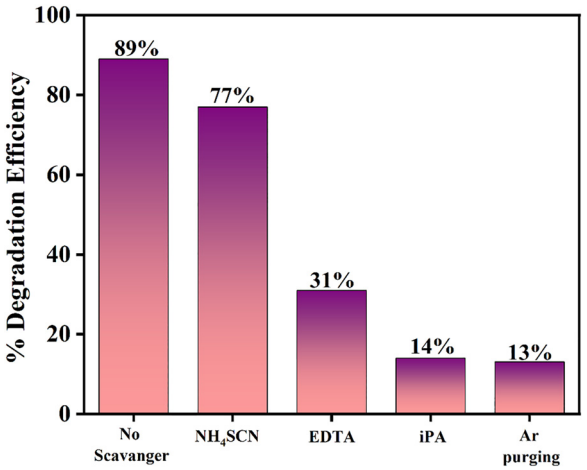

Fig. 12 Changes in degradation efficiency upon addition of NH_4SCN, EDTA, and iPA and Ar purging.

Proposed mechanism

The band edge potential values for gCN and BiOBr were calculated using the following equations:[58,59]

$$E_{VB} = \chi - E_e + 0.5E_g \quad (5)$$

$$E_{CB} = E_{VB} - E_g \quad (6)$$

where E_{CB} denotes the conduction band potential, E_{VB} denotes the valence band potential, χ denotes the electronegativity of the material, E_g represents the band gap energy, and E_e represents the energy of free electrons.

The calculated values for the VB and CB of gCN were +1.52 eV and −1.08 eV, respectively,[60] while their corresponding values for BiOBr were +3.20 eV and +0.69 eV[61] As presented in Fig. 11, BiOBr possesses a higher positive VB potential (+3.20 eV), compared to that of $^{\bullet}OH/H_2O$ (+2.68 eV), while the CB of gCN (−1.08 eV) has a larger negative potential than the standard redox potential of $O_2/O_2^{\bullet-}$ (−0.046 eV). The mechanism involving electron–hole pair recombination has been proposed in accordance with the aforementioned observations. Z-scheme heterojunctions were constructed where electrons undergo transition from the BiOBr valence band (VB) to its conduction band (CB), then migrate to

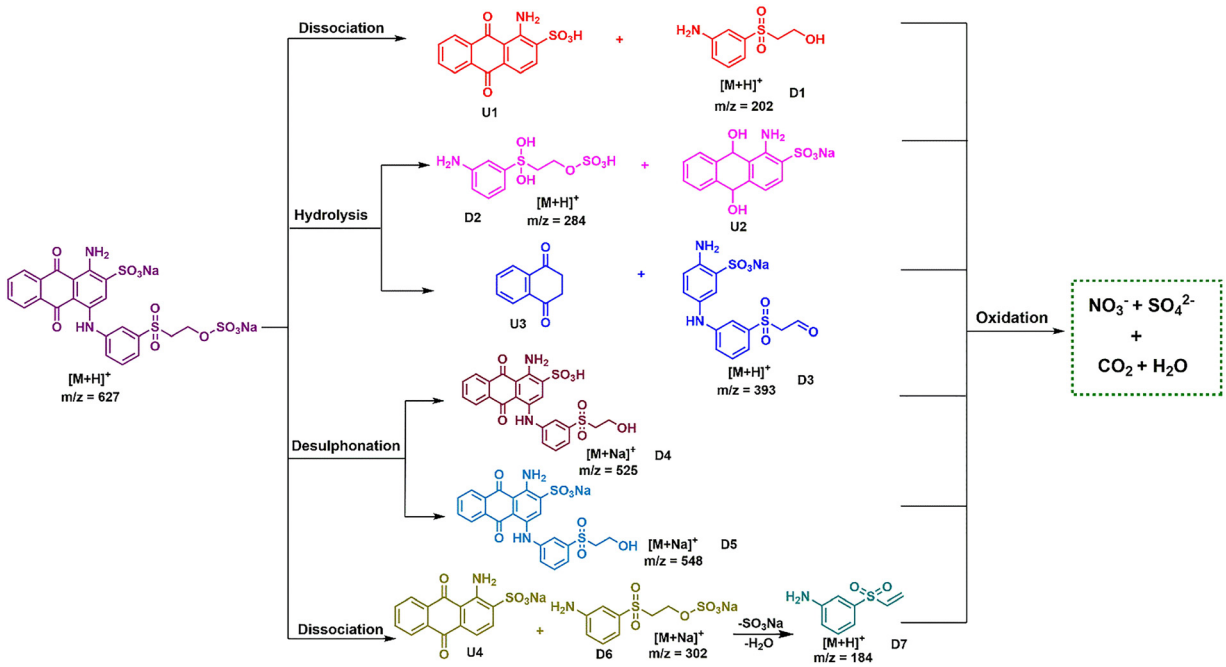

Scheme 1 Proposed mechanistic breakdown of RB19 using GB10 (D1–D7 depict detected fragments, and U1–U4 represent undetected fragments).

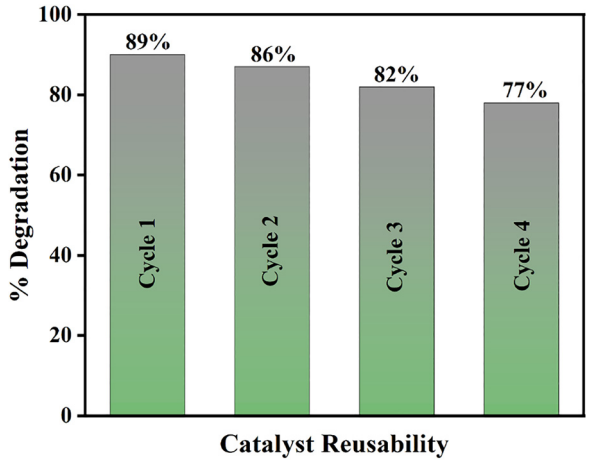

Fig. 13 Recyclability studies of GB10 towards photocatalytic degradation of RB19 up to 4 consecutive cycles.

the VB of gCN and then are excited to the CB of gCN, where they combine with the molecular oxygen to form superoxide anions, while the holes in the VB of BiOBr react with the water molecule and transform into a hydroxide radical. Hence, it is feasible to oxidise a water molecule to a hydroxyl radical and to reduce dissolved oxygen to a superoxide anion. Consequently, the reactive species convert the target pollutant (reactive blue 19) into its less hazardous products.[62]

HRMS studies

To obtain a deeper insight into the mechanism HR-MS studies were performed at two different intervals to identify the intermediates. The characteristic peak of protonated reactive blue 19 was detected at *m*/*z* 627. Furthermore, the different fragments (Scheme 1 and Fig. S8, S9) detected during the photocatalytic degradation process are represented by the signals at *m*/*z* 202 (D1), 284 (D2), 393 (D3), 525 (D4), 548 (D5), 302 (D6), and 184 (D7). It was found that as the reaction progresses, the relative peak intensity associated with smaller fragments increases, indicating photodegradation of RB19.

Scavenger studies

Several controlled investigations were performed to evaluate the role of reactive species. It was found that the photodegradation efficacy decreased from 89% to 77% with NH_4SCN. In addition, the efficiency declined to 31% with the addition of EDTA, which indicates the involvement of hole (h^+) scavengers in the mechanism and inhibits the formation of hydroxyl radicals from water. In addition, the efficiency decreases to 14% with the addition of iPA (Fig. 12), which suggests the participation of the hydroxyl radical ($^\bullet OH$). Additionally, the efficiency decreases to 13% after the Ar gas is purged from the reaction mixture for 15–20 minutes. This suggests that the Ar gas eliminates oxygen from the reaction, hence inhibiting the formation of superoxide anions. Thus, holes, superoxide anions, and hydroxyl radicals play a crucial role in the mechanism.

Reusability and stability of the photocatalyst

Stability and reusability are crucial for exploring possible future applications. The reusability of GB10 was assessed following its recovery from the reaction mixture and subsequent reuse under

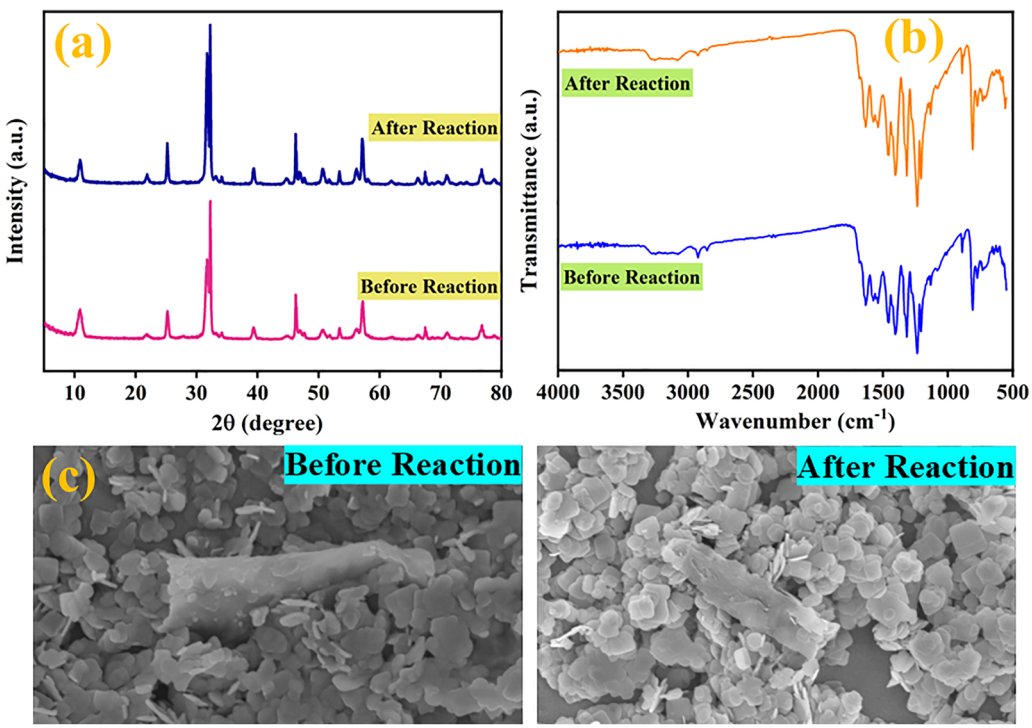

Fig. 14 (a) XRD patterns, (b) FTIR spectra, and (c) FESEM images of GB10 before and after reaction.

Table 2 Comparison of various reported catalysts' photocatalytic degradation performance towards reactive blue 19

S. no.	Catalyst	Catalyst dosage	Pollutant concentration (ppm)	Degradation efficiency (%)	Intensity of light (W m^{-2})	Time (min)	Light source	Ref.
1.	$Bi_5Nb_3O_{15}$/N-rGO	1 g L^{-1}	30	88	500	180	Visible	28
2.	$\alpha Fe_2O_3/WO_3$	1 g L^{-1}	10	95	254	360	Visible	29
3.	PmAP/rGO/MnO_2	0.5 g L^{-1}	20	90	125	120	Visible	30
4.	Bi_2MoO_6/Bi_2WO_6/MWCNTs	0.6 g L^{-1}	50	95	1000	240	Visible	31
5.	g-C_3N_4/BiOBr	1 g L^{-1}	60	~90	50	240	Visible	This work

identical conditions. It was determined that the degradation efficiency decreased by 77% between the first and fourth cycles, as illustrated in Fig. 13. Remarkably, the catalyst may have been lost during the washing stage, which would account for the 12% drop. Additionally, a variety of methods (XRD, FTIR, and FESEM) were employed to further assess the stability of GB10 after the photocatalytic reaction. It was observed that the XRD patterns and FTIR spectra of the recovered catalyst are almost identical with its as-synthesized analogue. Furthermore, the FESEM images showed that the morphology of the recovered catalyst remains practically similar to that of the original one (Fig. 14). Such observations confirm the high stability and reusability of the GB-10 photocatalyst.

Comparative analysis of degradation efficiencies

The prepared catalyst (GB10) was compared with the reported photocatalysts, and it was confirmed that GB10 demonstrated comparable photocatalytic degradation efficiency within comparable or smaller reaction time compared to the majority of the reported photocatalysts (Table 2). It was also observed that the majority of the catalysts require a greater intensity of light, a longer duration, and degrade a lower concentration of pollutant. GB10 is an optimal choice for the eradication of reactive dyes in wastewater due to its comparable degradation efficacy (~90%) within a comparable or smaller reaction time than most of the reported photocatalysts at a higher concentration of pollutant (60 ppm) with a lower intensity of light (50 Wm^{-2}).

Conclusion

The study reports the synthesis of g-C_3N_4/BiOBr with varying weight percentages *via* a hydrothermal approach for the photocatalytic elimination of RB19. Z-scheme heterojunctions were established, facilitating electron transfer. The control studies validate the involvement of hydroxyl radicals and holes in the mechanism. The HRMS confirms the photocatalytic degradation process through the generation of smaller fragments. The synthesised catalyst exhibited remarkable stability and reusability for up to four cycles. Consequently, owing to its reduced toxicity, straightforward synthesis, and affordability, the synthesised catalyst is deemed an exemplary choice for the removal of harmful contaminants from wastewater.

AI tools

The Grammarly tool has been used to verify and correct grammatical errors.

Author contributions

Kamya Jasuja: writing the original draft, visualization, validation, investigation, formal analysis, data curation, conceptualization; Raj Kumar Das: writing, review and editing, visualization, validation, supervision, resources, funding acquisition, conceptualization.

Conflicts of interest

The authors declare that they have no known competing financial interests or personal relationships that could have appeared to influence the work reported in this paper.

Data availability

The supporting data have been uploaded as part of the Supplementary information (SI). Supplementary information is available. See DOI: https://doi.org/10.1039/d5nj03536h.

Acknowledgements

This research is supported by the TIET VT CEEMS grant. The authors express their sincere appreciation to the Department of Physics and Material Science for contributing to performing XRD and SEM-EDS measurements and Sprint Testing Solutions for XPS and HRTEM analyses. The authors express sincere gratitude to DST-FIST (Infrastructure Grant number: SR/FST/CS-II/2018/69) for the HRMS facility. The authors extend their appreciation to Prof. Bonamali Pal and Prof. Satnam Singh for granting access to their laboratory facilities. The authors express gratitude to Dr Banibrata Maity and Ms Malika Phull for their contributions to the PL analysis. The authors extend their sincere appreciation to Prof. O.P. Pandey and Mr Abhishek Chandel for their contributions to EIS characterisation. The authors are very thankful to Prof. Kulvir Singh and Ms Navneet Mattu for providing the ICDD data.

References

1 A. P. Periyasamy, *Sustainability*, 2024, **16**, 495.
2 S. Vikal, Y. K. Gautam, S. Meena, V. Parewa, A. Kumar, A. Kumar, S. Meena, S. Kumar and B. P. Singh, *Nanoscale Adv.*, 2023, **5**, 805–819.
3 M. Rahman and Z. Tabassum, *Text. Leather Rev.*, 2024, **7**, 125–152.

4 R. Ahuja and R. Srivastava, *Nanoscale Adv.*, 2024, **6**, 3695–3698.
5 G. Samchetshabam, T. G. Choudhury and S. Gita, *Environ. Eco.*, 2017, **35**, 2349–2353.
6 A. K. Badawi, R. S. Salama and M. M. M. Mostafa, *RSC Adv.*, 2023, **13**, 19335–19355.
7 T. Adelpour, M. Amini, A. R. Shahverdi, S. Mojtabavi and M. A. Faramarzi, *Int. J. Biol. Macromol.*, 2024, **257**, 128493.
8 A. Chaturvedi, B. N. Rai, R. S. Singh and R. P. Jaiswal, *Rev. Chem. Eng.*, 2022, **38**, 617–639.
9 W. Chen, Z. Xing, N. Zhang, T. Cheng, B. Ren, X. Liu, Z. Wang, Z. Li and W. Zhou, *NPJ Clean Water*, 2024, **7**, 86.
10 V. Gadore, S. R. Mishra and M. Ahmaruzzaman, *Environ. Sci. Pollut. Res.*, 2023, **30**, 90410–90457.
11 J. J. Rueda-Marquez, I. Levchuk, P. F. Ibañez and M. Sillanpää, *J. Cleaner Prod.*, 2020, **258**, 120694.
12 K. Sekar, V. Balakumar, J. Uchida, T. Katsurao, H. Sakabe, B. Ohtani and K. Sasaki, *Environ. Res.*, 2022, **212**, 113635.
13 L. Jian, S. Li, H. Sun, Q. He, J. Chen, Y. Zhao and Y. Li, *Colloids Surf., A*, 2022, **652**, 129919.
14 A. Taneja, P. Gupta, S. Thatai, P. Khurana, K. R. Ranjan, J. Singh and M. Das Mukherjee, *J. Mol. Struct.*, 2024, **1318**, 139320.
15 E. Fernandes, J. Gomes and R. C. Martins, *Catalysts*, 2022, **12**, 1218.
16 M. Ikram, A. Shahzadi, S. Hayat, W. Nabgan, A. Ul-Hamid, A. Haider, M. Noor, S. Goumri-Said, M. B. Kanoun and S. Ali, *RSC Adv.*, 2022, **12**, 16991–17004.
17 N. Venkatesh, G. Murugadoss, A. A. A. Mohamed, M. R. Kumar, S. G. Peera and P. Sakthivel, *Molecules*, 2022, **27**, 7168.
18 P. Suja, J. John, T. P. D. Rajan, G. M. Anilkumar, T. Yamaguchi, S. C. Pillai and U. S. Hareesh, *J. Mater. Chem. A*, 2023, **11**, 8599–8646.
19 K. Sridharan, S. Shenoy, S. G. Kumar, C. Terashima, A. Fujishima and S. Pitchaimuthu, *Catalysts*, 2021, **11**, 426.
20 F. A. Alharthi, A. El Marghany, N. A. Y. Abduh and I. Hasan, *RSC Adv.*, 2023, **13**, 20417–20429.
21 A. B. Naveed, A. Javaid, A. Zia, M. T. Ishaq, M. Amin, Z. U. R. Farooqi and A. Mahmood, *ACS Omega*, 2023, **8**, 2173–2182.
22 S. Hassanzadeh, S. Farhadi and F. Moradifard, *RSC Adv.*, 2023, **13**, 10940–10955.
23 D. Li, W. Zhang, Z. Niu and Y. Zhang, *J. Alloys Compd.*, 2022, **924**, 166608.
24 X. X. Wei, B. Cui, X. Wang, Y. Z. Cao, L. B. Gao, S. Guo and C. M. Chen, *CrystEngComm*, 2019, **21**, 1750–1757.
25 D. Nakayama, C. M. Wu, K. G. Motora, P. Koinkar and A. Furube, *New J. Chem.*, 2023, **47**, 22078–22089.
26 S. Wang, G. Shen, Y. Yao and R. Sun, *RSC Adv.*, 2025, **15**, 12808–12813.
27 K. S. Lin, A. Furube, T. Katayama, P. Koinkar and C. M. Wu, *Mod. Phys. Lett. B*, 2025, **39**, 2441007.
28 B. Appavu, S. Thiripuranthagan and T. Sureshkumar, *Mater. Sci. Eng. B*, 2020, **252**, 114472.
29 M. Delnavaz, J. Farahbakhsh and S. S. Mahdian, *Water Sci. Eng.*, 2021, **14**, 119–128.
30 P. P. Mishra, N. Das, B. C. Tripathy and A. K. Behera, *New J. Chem.*, 2025, **49**, 14668–14680.
31 J. Tian, Z. Zhu and B. Liu, *Colloids Surf., A*, 2019, **581**, 123798.
32 S. Singh, N. Sharma, P. Sehrawat and S. K. Kansal, *Environ. Toxicol. Pharmacol.*, 2023, **99**, 104110.
33 M. Zhou, W. Huang, Y. Zhao, Z. Jin, X. Hua, K. Li, L. Tang and Z. Cai, *J. Nanoparticle Res.*, 2020, **22**, 13.
34 R. Manjupriya and S. M. Roopan, *Catalysts*, 2023, **13**, 308.
35 Z. Wang, B. Cheng, L. Zhang, J. Yu and H. Tan, *Sol. RRL*, 2022, **6**, 2100587.
36 J. Cao, J. Wang, Z. Wang, S. M. Zubairu, Y. Ding and G. Zhu, *Surf. Interfaces*, 2024, **45**, 103875.
37 B. Zhang, X. Hu, E. Liu and J. Fan, *Chin. J. Catal.*, 2021, **42**, 1519–1529.
38 D. Y. Liu, J. H. Dong, F. M. Liu, X. F. Gao, Y. Yu, S. B. Zhang, L. M. Dong and Y. K. Guo, *J. Ovonic Res.*, 2019, **15**, 239–246.
39 P. Rohilla, B. Pal and R. K. Das, *RSC Adv.*, 2025, **15**, 2347–2360.
40 V. Shinde, P. Tanwade, T. Katayama, A. Furube, B. Sathe and P. Koinkar, *Surf. Interfaces*, 2024, **46**, 104067.
41 G. Tang, F. Zhang, P. Huo, S. Zulfiqarc, J. Xu, Y. Yan and H. Tang, *Ceram. Int.*, 2019, **45**, 19197–19205.
42 S. S. Imam, R. Adnan, N. H. Mohd Kaus and M. H. Hussin, *J. Mater. Sci.: Mater. Electron.*, 2019, **30**, 6263–6276.
43 M. Singh, A. Kumar and V. Krishnan, *Mater. Adv.*, 2020, **1**, 1262–1272.
44 J. Lyu, Z. Hu, Z. Li and M. Ge, *J. Phys. Chem. Solids*, 2019, **129**, 61–70.
45 F. Chang, Y. Xie, C. Li, J. Chen, J. Luo, X. Hu and J. Shen, *Appl. Surf. Sci.*, 2013, **280**, 967–974.
46 P. Rohilla, B. Pal and R. K. Das, *J. Ind. Eng. Chem.*, 2025, **141**, 456–467.
47 A. Kundu, S. Sharma and S. Basu, *J. Phys. Chem. Solids*, 2021, **154**, 110064.
48 S. Singla, P. Devi and S. Basu, *Materials*, 2023, **16**, 5661.
49 Y. Wang, S. Zhao, Y. Zhang, J. Fang, Y. Zhou, S. Yuan, C. Zhang and W. Chen, *Appl. Surf. Sci.*, 2018, **440**, 258–265.
50 D. S. Vavilapalli, R. G. Peri, R. K. Sharma, U. K. Goutam, B. Muthuraaman, M. S. Ramachandra Rao and S. Singh, *Sci. Rep.*, 2021, **11**, 19639.
51 M. Dhillon, A. Naskar, N. Kaushal, S. Bhansali, A. Saha and A. K. Basu, *Nanoscale*, 2024, **16**, 12445–12458.
52 S. Vinoth and A. Pandikumar, *Renewable Energy*, 2021, **173**, 507–519.
53 X. Zhang, W. Li, L. Hu, M. Gao and J. Feng, *Nanomaterials*, 2024, **14**, 1071.
54 S. Chand, S. Mallick and A. Mondal, *Opt. Mater.*, 2025, **158**, 116463.
55 P. Intaphong, A. Phuruangrat, K. Karthik, P. Dumrongrojthanath, T. Thongtem and S. Thongtem, *J. Inorg. Organomet. Polym. Mater.*, 2020, **30**, 714–721.
56 Y. Hou, Y. Gan, Z. Yu, X. Chen, L. Qian, B. Zhang, L. Huang and J. Huang, *J. Power Sources*, 2017, **371**, 26–34.
57 Y. Yan, H. Yang, Z. Yi, T. Xian and X. Wang, *Environ. Sci. Pollut. Res.*, 2019, **26**, 29020–29031.
58 F. Qiu, W. Li, F. Wang, H. Li, X. Liu and J. Sun, *J. Colloid Interface Sci.*, 2017, **493**, 1–9.

59 L. Jian, S. Li, H. Sun, Q. He, J. Chen, Y. Zhao and Y. Li, *Colloids Surf., A*, 2022, **652**, 129919.
60 Z. Zeng, K. Li, T. Yuan, Y. Liang, J. Yang, G. Yang, K. Wang and Z. Xiong, *J. Mater. Sci.: Mater. Electron.*, 2021, **32**, 9972–9989.
61 A. Meng, W. Li, Z. Li and J. Zhang, *Catalysts*, 2024, **14**, 548.
62 P. Soni, B. Pal and R. K. Das, *Nanoscale Adv.*, 2025, **7**, 3055–3067.